ISSN (Print) 1226-1750
ISSN (Online) 2233-6656
Journal of Magnetics 28(2), 108-123 (2023) https://doi.org/10.4283/JMAG.2023.28.2.108

Research on Magnetic Actuation Mechanism and Kinematics of Soft Inspection Robot for HVDC Transmission Line

Xianjin Xu[1]*, Yanhao Huang[1], Lanlan Liu[2], Yu Yan[2], Haifeng Yan[1], and Yuhang Yang[1]

[1]*Hubei University of Technology, College of Mechanical Engineering, Hubei Wuhan 430068, China*
[2]*State Grid Hunan Electric Power Company Live Line Inspection and Intelligent Work Technology State Grid Corporation Laboratory, Hunan Changsha 410004, China*

(Received 27 September 2022, Received in final form 31 March 2023, Accepted 4 April 2023)

Currently, most of the inspection robots for high-voltage transmission lines, both at home and abroad, utilize a multi-cantilever rigid structure. However, the inefficiency and poor safety of these robots when it comes to crossing obstacles make them impractical. To address this issue, a magnetically actuated soft inspection robot has been developed. This robot uses the amperage force applied to the current-carrying coil in a HVDC toroidal magnetic field to efficiently and flexibly cross multiple obstacles in an inchworm-like motion. The focus of this paper is on the design and theoretical calculation of the magnetically actuated model, specifically the magnetic linear traction force and magnetic adsorption force (diastolic force), required to enable the soft robot to crawl. Through simulation and kinematic analysis, the results show that the magnetically actuated soft robot design proposed in this paper is theoretically feasible, providing a foundation for future developments in magnetically actuated soft robots.

Keywords : HVDC, soft inspection robot, magnetic actuation, creeping over obstacle, simulation, kinematics

1. Introduction

The electric power system is a vital foundation for the smooth operation of modern human society. Currently, the inspection of transmission lines is predominantly carried out manually. However, due to the complex terrain and harsh environments in which high-voltage transmission lines are erected, manual inspections are challenging and inefficient. Advancements in technology and the economy have led to the use of drones and helicopters equipped with cameras to assist workers in inspections. Despite the benefits, this approach remains expensive, has inspection blind spots, and is susceptible to weather and wind loads. With the development of the intelligent robotics industry, the use of robots for high-voltage transmission line inspection has become a new trend with a view to improving the efficiency and accuracy of high-voltage line inspection. However, currently developed inspection robots such as Expliner [1] from Japan (Fig. 1(a)), LineScout [2-4] from Canada (Fig. 1(b)), Keystar [5] developed by Wuhan University in collaboration with Keystar intelligence robot co. ltd and AApe-C2 series inspection robots [6] designed by Shenyang Institute of Automation, Chinese Academy of Sciences are all multi-cantilever rigid robots, these robots are complex in structure, large in size, inefficient, and pose significant safety risks while crossing obstacles, as illustrated in Fig. 1. To overcome these limitations, the incorporation of soft robotics - a field that offers redundant degrees of freedom and flexible deformation - into high-voltage line inspection is a promising new direction for development [7-12]. Compared to traditional rigid robots, soft robots are more suitable for overhead high-voltage line inspection, which is a complex working environment. By employing soft inspection robots, obstacles can be more efficiently and safely traversed, ultimately leading to improved performance and reduced robot size. To this end, we propose a novel approach for high-voltage line inspection using a magnetically actuated inchworm bionic soft robot, building on previous work on a three-armed magnetically actuated inspection robot [13, 14]. By utilizing the Ampere force generated in the circular magnetic field around the high-voltage DC wire using a current-carrying coil [15], the soft robot is driven to move in an "Ω" shaped motion, enabling it to

*Corresponding author: Tel: +86-132-8382-4898
Fax: +86-027-5970418, e-mail: xxjoyjn@162.com

(a) Expliner

(b) LineScout

Fig. 1. (Color online) Multi-cantilever rigid inspection robot.

(a) Anti-vibration hammer

(b) Spacer

Fig. 2. High-voltage transmission line obstructions.

efficiently and flexibly cross obstacles, thereby improving the efficiency and reliability of obstacle-crossing.

2. Inspection Robot Operating Environment Characteristics and Simulation

2.1. Operating environment

Traditional obstacles encountered on high-voltage overhead transmission lines include anti-vibration hammers, and due to the requirement of multiple splices in the setup of HVDC transmission lines, spacers are also necessary [16] as depicted in Fig. 2. The connection structure of such fixtures and transmission lines pose a challenge for conventional wheeled multi-cantilever rigid robots to roll through, thus conventional rigid robots mostly rely on climbing and other complex, inefficient and time-consuming methods to cross barriers.

2.2. Simulation of magnetic field around high-voltage lines

The proposed magnetically actuated approach in this paper is rooted in the assumption that the magnetic field surrounding a HVDC conductor takes on a toroidal shape [17]. However, the presence of various fixtures or obstacles installed on the conductor may alter the magnetic field characteristics. Thus, it is necessary to analyze the magnetic field surrounding these obstacles to validate the feasibility of the aforementioned hypothesis.

As shown in Fig. 3, when there are no obstacles around a single wire, the magnetic field takes on a ring-like shape. Even in the presence of obstacles such as anti-vibration hammers and spacers installed around the high-voltage conductor, the magnetic field remains in a ring shape. However, the presence of four split wires shows slight interference as the magnetic fields of the four wires affect each other, causing the magnetic field around the four wires in the simulation results to shift slightly outward along the diagonal of the four split wires, its effect is small enough to be ignored. These simulation results serve to confirm the hypothesis that the magnetic field around a single high-voltage DC conductor is indeed toroidal.

The 500 kV DC transmission line typically employs four split conductors, whose cross-sectional views are illustrated in Fig. 4, and the direction of the four wire currents is consistently outward. The center of the high-voltage line cross-section A serves as the center of a circle with a radius of d0, which is denoted as point O.

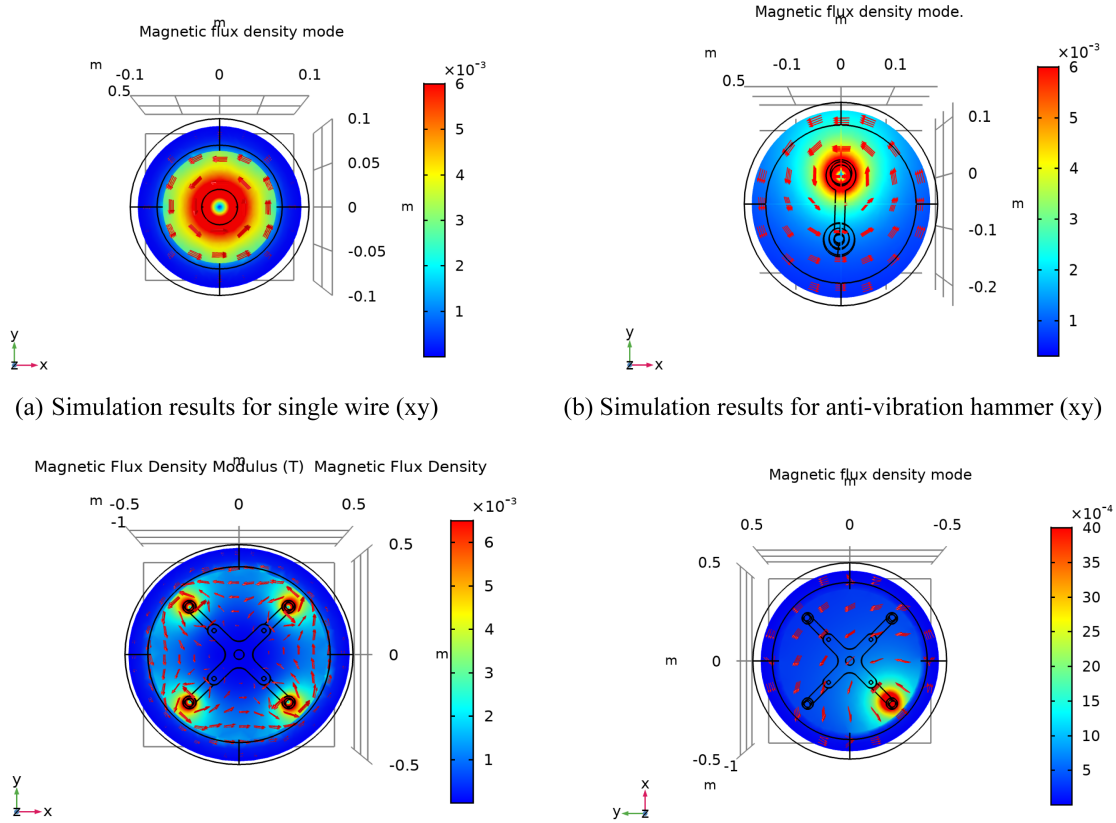

(a) Simulation results for single wire (xy)

(b) Simulation results for anti-vibration hammer (xy)

(c) Simulation results for four split spacer (xy)

(d) Simulation results for single wire in four-split spacer (xy)

Fig. 3. (Color online) The magnetic flux density mimicry results for different obstacle situations.

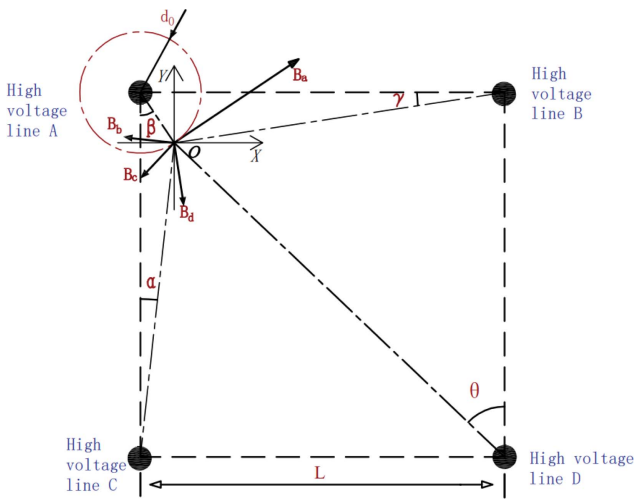

Fig. 4. (Color online) Schematic diagram of the magnetic field in the section of the four-split wire.

Point O is located at an angle of β with respect to the vertical direction of the high-voltage line A, while the high-voltage line B is situated at an angle of α in the same direction. The angle between the line connecting point O and high-voltage line D, and the horizontal direction is γ. The angle between the line connecting point O and high-voltage line C, and the vertical direction is θ. With point O as the circle's center, a rectangular coordinate system is constructed, where *Ba*, *Bb*, *Bc*, and *Bd* represent the magnetic induction strengths of high-voltage lines A, B, C, and D, respectively, at point O.

The magnetic induction intensities B_a, B_b, B_c, and B_d are projected on the X-axis and Y-axis to obtain the respective components. From the Biot-Savart theorem, the expressions of the magnetic induction strengths B_a, B_b, B_c, and B_d are:

$$B_{ay} = \frac{U_0 I}{2\pi L_{OA}} \cdot \sin\beta \qquad B_{by} = \frac{U_0 I}{2\pi L_{OB}} \cdot \sin\alpha$$
$$B_{cy} = \frac{U_0 I}{2\pi L_{OD}} \cdot \sin\theta \qquad B_{dy} = \frac{U_0 I}{2\pi L_{OC}} \cdot \cos\gamma \tag{1}$$

$$\cos\beta = \frac{L^2_{OA} + L - L^2_{OB}}{2 \cdot L_{OA} \cdot L} \qquad \cos\alpha = \frac{L - \cos\beta \cdot L_{OA}}{L_{OB}}$$
$$\cos\gamma = \frac{L - \sin\beta \cdot L_{OA}}{L_{OD}} \qquad \cos\theta = \frac{L - L_{OA} \cdot \cos\beta}{L_{OC}} \tag{2}$$

The combined magnetic field of magnetic induction on the Y-axis is:

$$B_y = B_{ay} + B_{by} + B_{cy} + B_{dy} \tag{3}$$

In this scenario, the vacuum permeability (U0) is equal to $4\pi \times 10^{-7}$ H/m. The high-voltage line has a current of $I = 1000A$, and the maximum distance between the current-carrying coil and the high-voltage line is $d_0 = L_{OA} = 0.02$ m. Ky represents the ratio of the combined magnetic induction of the high-voltage conductor on the Y-axis to the magnetic induction of the high-voltage line A on the Y-axis.

$$K_y = \frac{B_y}{B_{ay}} = \left[1 + \frac{L^2_{OA}}{L^2_{OB}} - \frac{L^2_{OA}}{L^2_{OD}} + \left(\frac{L \cdot L_{OA}}{L^2_{OD}} + \frac{L \cdot L_{OA}}{L^2_{OC}} - \frac{L^2_{OA} \cdot \cos\beta}{L^2_{Oc}}\right)\frac{1}{\sin\beta}\right] \tag{4}$$

$$\begin{aligned} &L = 0.4m \quad L_{OB} \in [0.38, 0.42] \\ &L_{OC} \in [0.546, 0.566] \quad L_{OD} \in [0.38, 0.42] \end{aligned} \tag{5}$$

Bringing into the formula gives $K_y \approx 1$, so the high-voltage line in the Y-axis direction of the combined magnetic field strength and high-voltage line A in the Y-axis direction of the magnetic field strength in the size of very close; Similarly, the high-voltage line in the X-axis direction of the combined magnetic field strength and high-voltage line A in the X-axis direction of the magnetic field strength in the size of very close. This indicates that the magnetic field produced by high-voltage lines B, C, and D has minimal impact on the magnetic field created by high-voltage line A. Both the calculation and simulation outcomes confirm that the interference among the magnetic fields of the four wires in the quadruple split conductor is negligible, further validating the theory that the magnetic field surrounding a single HVDC conductor takes on a toroidal shape.

3. Magnetically Actuated Soft Inspection Robot Barrier Crossing Structure Design

3.1. Magnetically actuated soft inspection robot configuration

The robot's exterior structure comprises a soft inchworm bionic body shell, while the internal functional components include a duo of magnetic adsorbers, a pair of magnetic linear actuators, and a peristaltic soft body made of polyurethane. Please refer to Fig. 5 for a visual representation.

The functional structure of the robot contains magnetic attractors positioned at either end, which generate magnetic attraction or tensioning forces. Similarly, magnetic linear actuators are also located at both ends, producing magnetic linear traction forces. The robot can crawl across

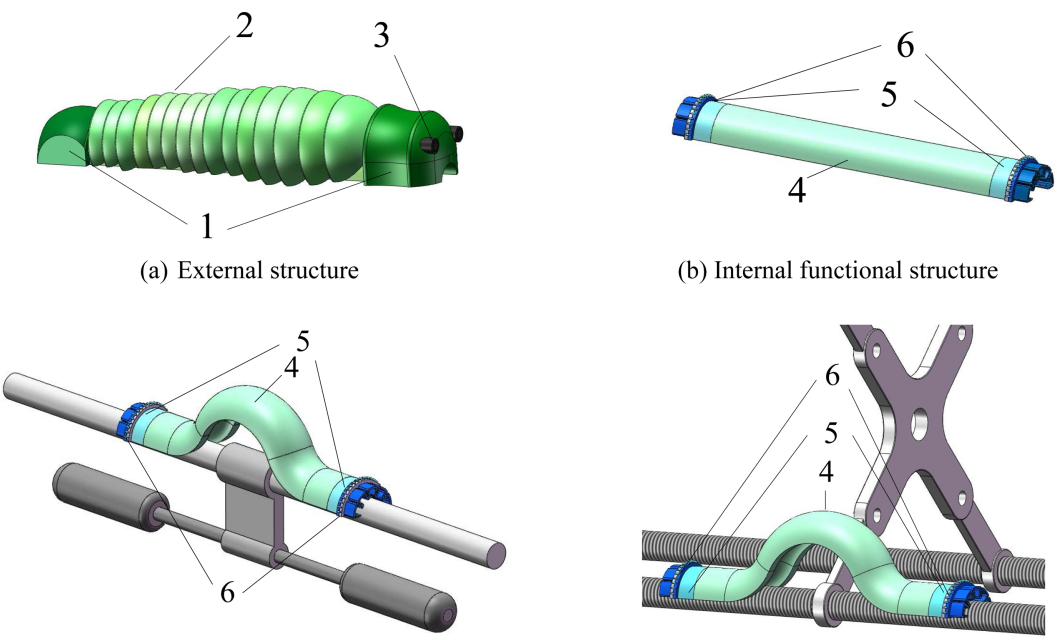

(a) External structure (b) Internal functional structure

(c) Crossing Obstacles (Anti-vibration hammer) (d) Crossing Obstacles (Spacer)

1. Head shell; 2. Soft body shell; 3. Binocular camera
4. Peristaltic soft body; 5. Magnetic adsorber; 6. Magnetic linear actuator.

Fig. 5. (Color online) Robot structure.

anti-vibration hammers and spacer bars by employing the joint action of magnetic adsorption force (or diastolic force) and magnetic linear traction force. Given the high tension wire's diameter of $d = 0.04$ m, the peristaltic body's outer diameter of $r_1 = 0.046$ m, inner diameter of $r_2 = 0.024$ m, the magnetic peristaltic soft body's length of $a = 0.2$ m, and the polyurethane density of $p = 1.1$-1.25 kg/m^3, the peristaltic soft body has a mass of $m = 1.06$ kg. As a result, the robot's total mass is approximately 1.5 kg.

3.2. Magnetically actuated soft inspection robot crossing obstacles action planning

When the magnetically actuated soft inspection robot encounters an obstacle, it simulates the motion of an inchworm crawling [18]. The initial posture of the inchworm is flat and straight, and the inchworm's motion cycle comprises two states. In the first state, the head of the inchworm grasps while the tail end relaxes and lifts for contraction, as depicted in Fig. 6(a). In the second state, the hind end of the inchworm grasps the branch, releases the head, and stretches forward to straighten the trunk part, as illustrated in Fig. 6(b). Finally, the entire body returns to the initial flat state.

The magnetically actuated soft body inspection robot in this paper plans its crossing action by leveraging the above three magnetic field forces (taking the crossing of anti-vibration hammer as an example).

In the barrier-free section, the magnetically actuated soft body inspection robot relies on the linear traction forces F1 and F2 generated by the magnetic linear actuators at both ends and the adsorption forces F3 and F5 generated by the magnetic absorbers at both ends to make the robot travel stably along the high-voltage line in a straight line. However, when encountering an obstacle, the current in the front linear actuator's coil is turned off, causing F2 to disappear while increasing F3 and F5. Consequently, the robot compresses the middle soft body under the influence of F1. Afterward, by altering the magnetic adsorber and magnetic linear actuator's coil current direction at the front end, F5 and F2 alter to the opposite direction, while the robot's front portion gradually suspends in the air. As the robot advances with the assistance of F1, the magnetic linear traction forces F2 and F5 are terminated, enabling the front end of the peristaltic soft body to cross the obstacle in the air under its own reaction force. The current direction of the coil in the magnetic absorber is then changed back to the positive direction, resulting in the generation of the adsorption force F5, which is directed vertically downward, along with the robot's own gravity. This combination of forces enables the front end of the robot to return to the high-voltage line. The second half of the robot then repeats the same sequence of movements as the front end to complete the crawl-over action, as depicted in Fig. 7.

3.3. Research on linear actuation mechanism of magnetically actuated soft body inspection robot

The magnetic field generated by HVDC current is not strong enough to produce the required current in the magnetic core's coil. Therefore, it is necessary to use the magnetic congregating effect of powerful magnetic materials to enhance the magnetic field generated around the wire. The magnetic core in the magnetic linear actuator is divided into two layers, one made of strong magnetic material and the other made of weak magnetic material. The long side L_1 of the coil is placed in the strong magnetic material while the other long side L_2 is placed in the weak magnetic material, as illustrated in Fig. 8(a). According to the left-hand rule, a current carrying coil in a magnetic field can generate determined direction Ampere forces $F1$ and $F2$, whose resultant force is the force received by the robot as a whole in the direction of its movement. Since strong magnetic materials have a strengthening effect on the weak magnetic field around the high-voltage line, $F1$ will be much larger than $F2$. Therefore, $F_a \approx F1$, $F1$ is considered as the traction force

(a) First state (b) Second state

Fig. 6. (Color online) The "Ω" motion of an inchworm crawling.

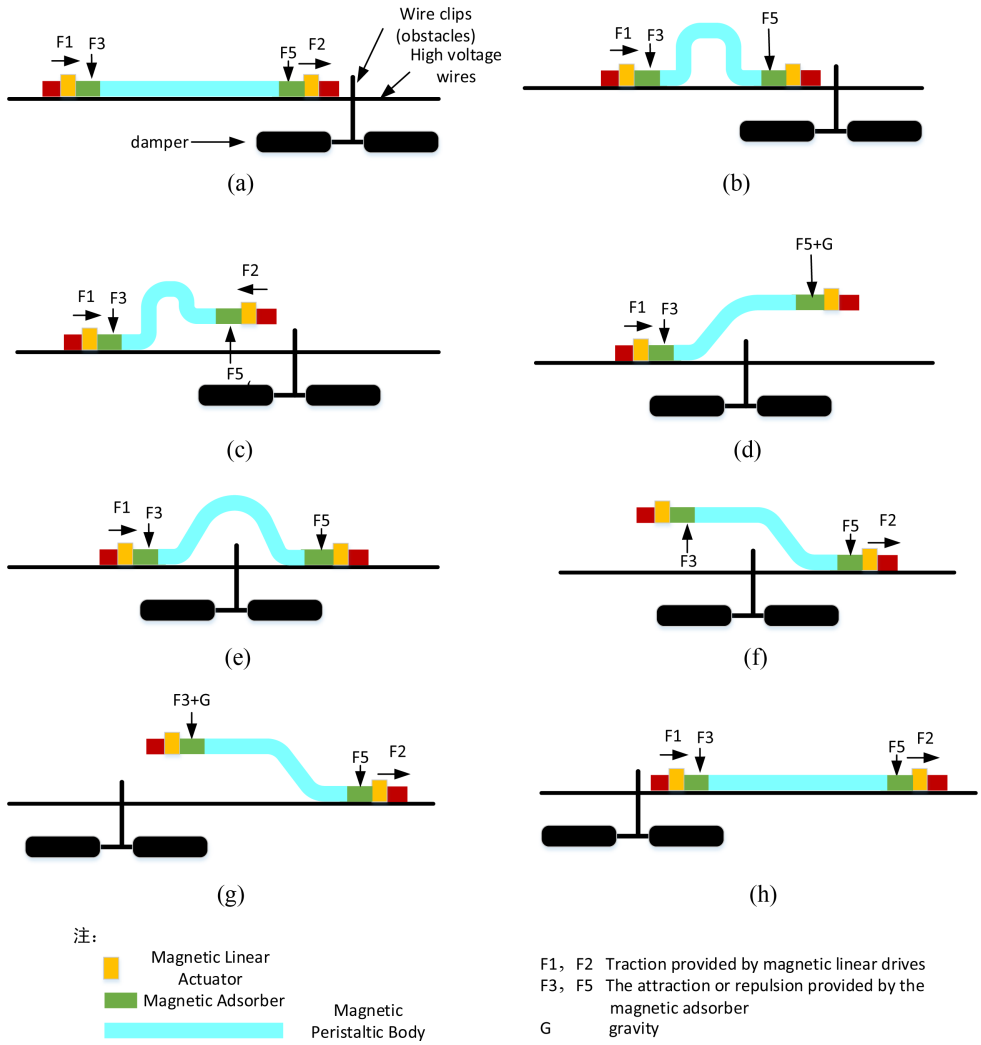

Fig. 7. (Color online) Magnetically actuated soft inspection robot creeping across the anti-vibration hammer action planning.

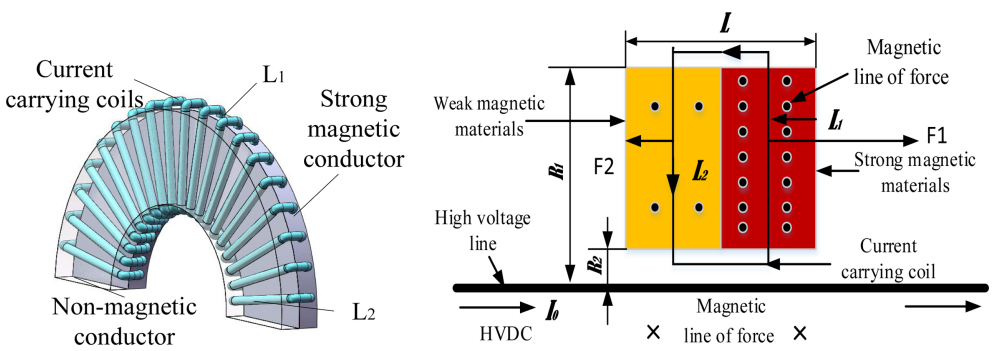

(a) Magnetic linear actuator model (b) Magnetic linear actuator working mechanism

Fig. 8. (Color online) Structure and working mechanism of magnetic linear actuator.

in the direction of robot motion.

The magnetic field strength at any point located at a distance of r from the center of the wire in a strengthened magnetic field is:

$$B = \frac{u_0 u_r I_0}{2\pi r} \tag{6}$$

I_0 - High voltage line current; u_0 - Magnetic permeability in vacuum; u_r - Relative permeability of strong permeable magnets.

Set the current in the coil as I_1, then the ampere force $F1$ is:

$$F1 \approx \int_{r_2}^{r_1} \frac{u_0 u_r I_0}{2\pi r} I_1 dr \tag{7}$$

I_1 = 10A, I_0 = 1000A, r_2 = 0.024 m, r_1 = 0.046 m, u_0 = $4\pi \times 10^{-7}$, to take $u_r = 1000$, the calculations are performed with the number of turns of the coil being 10, 20, 30, and 40, respectively. When the number of turns is set to 30, the ampere force of a single magnetic linear driver is : F_a = 39N. The entire robot can be provided with a linear drive force of 78N.

3.4. Research on the adsorption (relaxation) mechanism of magnetically actuated soft inspection robot

The magnetic adsorber consists of a magnetic core comprising of two layers of distinct materials. The layer adjacent to the high-voltage wire is made up of strong magnetic material to enhance the magnetic field generated by HVDC, while the other layer is composed of weak magnetic material. The two elongated sides of the coil carrying the current are individually placed in these two material layers, and the ampere force exerted on the coil in the HVDC magnetic field serves as the stretching or adsorption force to propel the soft body, as illustrated in Fig. 9(a).

The Fig. 9(b) illustrates a high-voltage line where the current flows inward perpendicular to the paper, generating a circular magnetic field B around it. The two long sides of the coil are subjected to ampere forces $F1$ and $F2$ of different magnitudes in opposite directions, and the ampere force $F1$, which is generated in the magnetic field after reinforced by strong magnetic material, is much larger than $F2$. The ampere force generated by placing the short side of the coil in the air is small and in opposite directions, Consequently, the resultant force Fb of the entire coil is roughly equivalent to $F1$.

The strength of the reinforced magnetic field can be calculated using equation (6), where L is the length of the coil. The long side of the coil is always perpendicular to the direction of the magnetic field. The ampere force acting on the long side of the coil placed in the strong magnetic material can be expressed as:

$$F1 = BIL = \frac{u_0 u_r I_0}{2\pi r} I_1 L \tag{8}$$

$ur = 1000$, $I_A = 10$A, $I_0 = 1000$A, $r = 0.024$ m, $L = 0.1$ m, the calculations are performed with the number of turns of the coil being 10, 20, 30, and 40, respectively. When the number of turns is set to 30, the magnitude of the adsorption force is: $F_b = 250$N.

Using a coil with 10 or 20 turns results in an adsorption force that is too weak and cannot guarantee the robot's safety. On the other hand, a coil with 40 turns will make the inner coil of the magnetic core too dense, Therefore, 30 turns coil is a more suitable choice. When the magnetically actuated soft inspection robot is crawling over an obstacle, it is necessary to keep at least one magnetic adsorber attached to the high-voltage line. Even in this extreme scenario, the 30-turn coil's 250N adsorption force is sufficient to ensure that the robot remains attached to the high-voltage line. Furthermore, the magnetic adsorber is capable of providing a relaxing force. By reversing the direction of the current in the current-carrying coil, a relaxing force of 250 N can be generated, which is enough to allow the head, tail or peristaltic soft body of the robot to relax offline. These forces ensure that the robot can successfully complete the entire process of crawling over obstacles.

4. Magnetically Actuated Simulation Analysis

4.1. Magnetic core analysis of magnetic linear actuator

Theoretical calculations were used to determine the

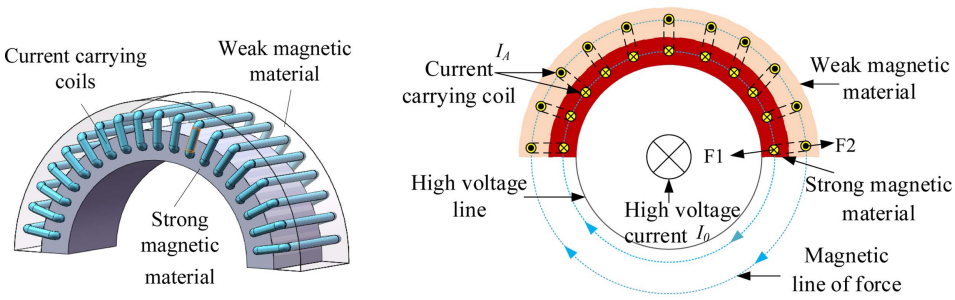

(a) Magnetic adsorber model (b) Magnetic adsorber working mechanism

Fig. 9. (Color online) Structure and working mechanism of magnetic adsorber.

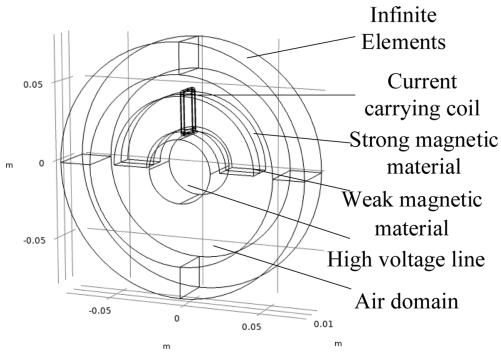

Fig. 10. Equivalent model of actuator coil.

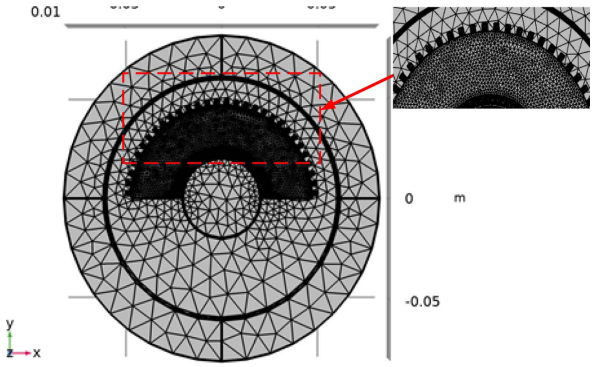

Fig. 11. Mesh division result of 30-turn coil.

necessary requirements, which were then verified through simulation analysis. To simulate the linear traction of a magnetically actuated soft inspection robot on an unobstructed section of a high-voltage line, an equivalent model must first be created. The current-carrying coil, wound with multiple turns of thin wire, each turn of the coil can be equivalent to a rectangular coil. This model was created using COMSOL simulation software, as depicted in Fig. 10. The model comprises a central cylinder (representing the high-voltage line), a semi-circular magnetic core (made up of half strong magnetic material and half weak magnetic material), and a larger cylinder (representing the air domain).

Once the model is optimized, the optimal range for each parameter is determined, the magnetically actuated soft body inspection robot drive core parameters are instantiated. Finally, a simulation analysis is performed. To create the simulation model, the radius of the high voltage line is set as $r_1 = 0.02$ m, the radius of the air domain as $r_2 = 0.03$ m, and an infinite elementary domain is divided in the air domain with a thickness of 0.05 m. To create the simulation model in COMSOL Multiphysics software, the high voltage line and air domain are set to a height of $h_1 = 0.02$ m, while the magnetic core has an outer circle radius of $r_a = 0.046$ m, an inner circle radius of $r_b = 0.024$ m, and a height of $h_2 = 0.02$ m. The magnetic core is split from the middle using an XY working plane, with one half made of strong magnetic material and the other half made of weak magnetic material which can be equated to air in the simulation. A rectangular coil is then drawn in the XZ-plane and stretched in both directions, with a coil cross-section of $(0.001 \times 0.001\pi)$ m^2. The appropriate materials are added to each part of the model as outlined in Table 1.

The selected physical field is magnetic field (mf), and boundary conditions are set. Given a current of I_h=1000A in the high-voltage line, the external current density of the high-voltage line is set to $(1000/0.02 \times 0.02\pi)A/M^2$ The coil current is set to $I_l = 10$A, the material type is selected from the materials library, the wire type is uniform multi-turn, the coil type is numerical, the coil excitation type is current, the coil wire conductivity is $\sigma_{coil} = 5.998$[S/m], and the coil cross-sectional area is $a_{coil} = (0.001 \times 0.001\pi)$ m^2. Boundary conditions are set for force calculation, and all coils are selected.

Finally, the model is meshed using the free tetrahedral mesh. The current-carrying coil part is first meshed using a highly refined mesh, and the magnetic core part is meshed using a finer mesh. The remaining parts are meshed using a conventional mesh. The meshing results are shown in Fig. 11.

The research is conducted under steady-state conditions, with a simulation calculation for 30 turns of the coil. The simulation results are then compared with the theoretical calculation values to ensure accuracy. The results of the simulation are depicted in Fig. 12 and Fig. 13.

The magnetic field density model in Fig. 12 shows a

Table 1. Model materials and their properties.

Material Name Properties	High Voltage Line (SteelAISI 4340)	Strong magnetic material	Current carrying coil [Soft Iron(with losses)]	Air domain (Air)
Electrical conductivity (S/m)	4.032×10^6	0	1.12×10^7	0
Relative magnetic permeability	1	1000	1	1
Relative dielectric constant	1	1	1	1

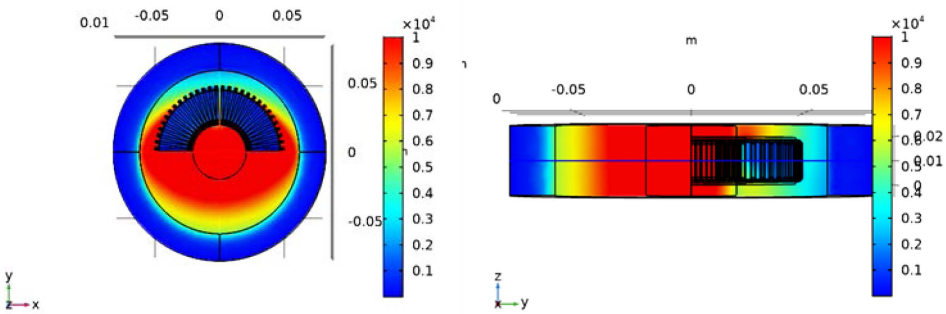

(a) Simulation result of 30-turn coil (xy) (b) Simulation result of 30-turn coil (yz)

Fig. 12. (Color online) Nephogram of simulation results of magnetic linear actuator 30 turn coil magnetic core.

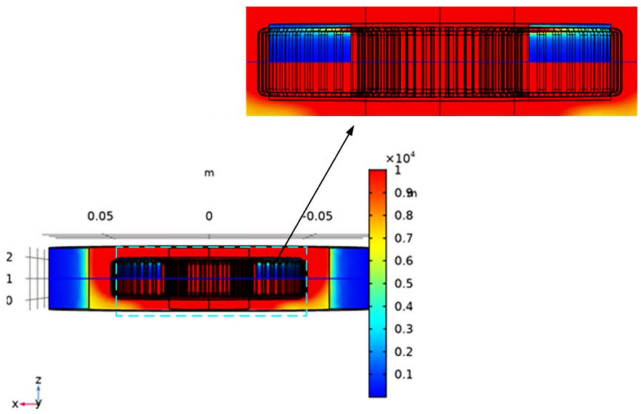

Fig. 13. (Color online) 30 turn coil partial enlargement.

significant enhancement of the coil's flux density due to the magnetic core. As seen in Fig. 12(a), the energized coil embedded in the core partially absorbs the magnetic field around the high-voltage line, thus suppressing its outward dispersion. Moreover, the strength of the magnetic field near the short side of the energized coil, close to the high-voltage line, is much higher than the side away from it. In Fig. 13, the xz plane of the 30-turn coil reveals that the magnetic field at the end of the strong magnetic material is much higher than that of the weak magnetic material.

Calculate the magnitude of the ampere force on the x, y and z axes by simulating a 30-turn coil:

F_x = -0.16N, F_y = 2.08N, F_z = -35.41N.

Based on the simulation results, it can be concluded that a small Ampere force respectively exists on the x and y axes direction. This is attributed to the magnetic coupling in the magnetic drive system, causing a shift in the magnetic induction line, resulting in a component force in the x and y axis directions. However, the component force is much smaller than the Ampere force in the z-axis direction, so its impact is negligible. The comparison between the simulated and theoretical values of the Ampere force in the z-axis direction of the magnetic core shows that there is still some error between them, but the error is minimal, which confirms the validity of the magnetically actuated theory.

4.2. Magnetic core analysis of magnetic adsorber

The amperage force generated by the magnetic adsorber core is mainly studied in the direction perpendicular to the upward direction of the soft robot. Construct the magnetic core model, take the radius of high voltage line r_0 = 0.02 m, the inner diameter of this core model r_1 = 0.024 m, the outer diameter r_2 = 0.034 m, and the radius of the coil in the magnetic core r = 0.002 m, as shown in Fig. 14. The material properties refer to Table 1 model materials and their properties in the previous section, set the boundary conditions of model, the high voltage line material and current settings are the same as in the magnetic linear actuator, and set the relative permeability of the strong magnetic core material to 1000.

In this model, the coil part requires a customized mesh since the system's default extremely fine mesh cannot

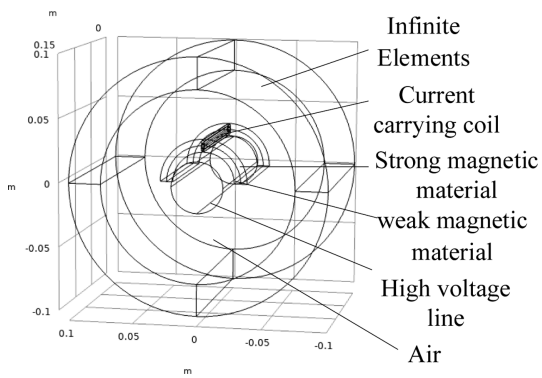

Fig. 14. Equivalent model of magnetic adsorber core.

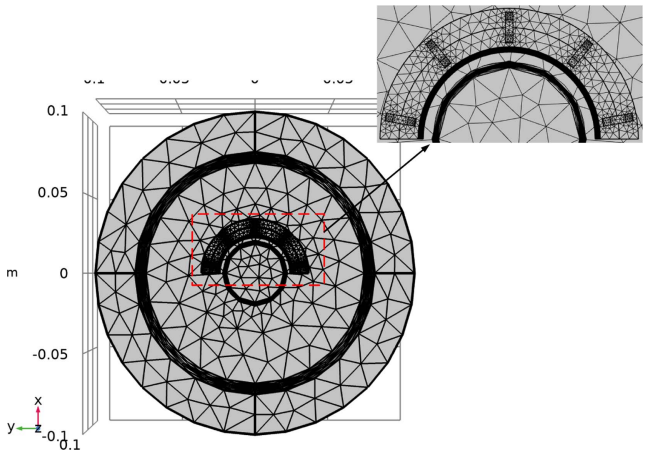

Fig. 15. (Color online) Magnetic adsorber meshing result.

meet the requirements. The maximum cell size of the coil mesh is set to 2.7 cm, while the minimum cell size is set to 0.012 cm. The remaining parts are divided using the conventional mesh set by the system, and the resulting mesh is shown in Fig. 15.

For this magnetic core, it was proposed to select 30 turns for the coil. The flux density distribution of the coil was obtained through several simulation iterations, which are shown in Fig. 16.

From the simulation results depicted in Fig. 16(a), it is evident that the strong magnetic material has a magnetic gathering effect on the weak magnetic field around the high-voltage line, thereby curbing the dispersion of the toroidal magnetic field surrounding the high-voltage line. By selecting 30 turns for the coil, the coils in the magnetic core are placed in the most compact arrangement. The outcomes of the aforementioned coils are subjected to post-processing to determine the magnitude of the ampere force generated by the 30-turn coil along the x, y, and z axes.

$F_x = 243.40\text{N}$, $F_y = 2.41\text{N}$, $F_z = -1.38\times10^{-3}\text{N}$.

Due to the coupling effect of the magnetic field, there is a shift in the magnetic induction lines, resulting in a component force in the y-axis and z-axis. However, this force is negligible due to its small magnitude. The simulation results show very small errors when compared to the theoretical values derived from Equation (9), which proves the accuracy of the magnetic adsorption model.

5. Kinematic Analysis of The "Ω" Motion of Magnetically Actuated Soft Inspection Robot

5.1. Magnetically actuated soft inspection robot posture analysis

After the correctness of the magnetic actuation theory was confirmed through magnetic field simulation and theoretical calculations, it was necessary to perform a kinematic analysis of the soft inspection robot to verify the feasibility of the "Ω" motion for creeping over obstacles. The motion curve of the soft robot during the "Ω" motion is a unique curve that can be divided into three parts, each with a different bending direction but the same curvature. As a result, the kinematic model of the

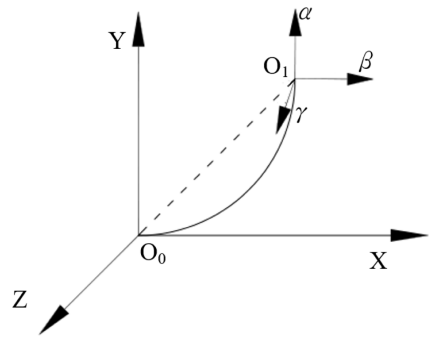

Fig. 17. Sketch of robot structure in spatial coordinate system.

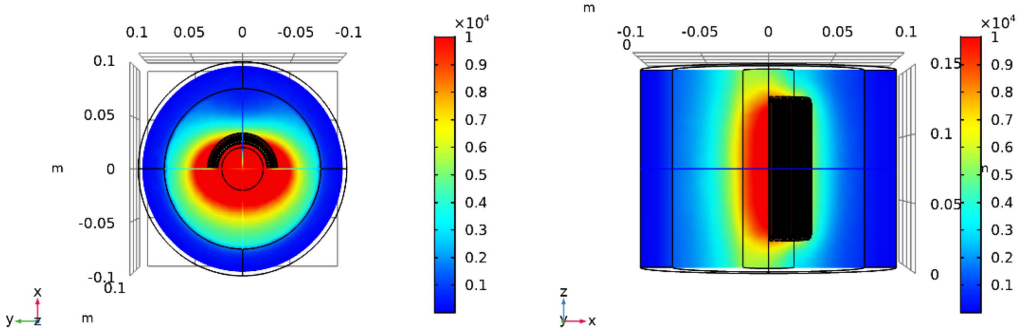

(a) Simulation result of 30-turn coil (xy) (b) Simulation result of 30-turn coil (xz)

Fig. 16. (Color online) Nephogram of simulation results of magnetic adsorber 30 turn coil magnetic core.

soft robot's "Ω" motion can be solved using a simplified method. Fig. 17 illustrates a sketch of the robot in the spatial coordinate system.

The posture of any point x on the curve in the figure is expressed as:

$$\mathbf{x}(s) = \left[x(s), y(s), 0\right]^T \tag{9}$$

At the specific point of motion during the "Ω" movement, the unit tangent vector, principal normal vector, and binormal vector can be utilized to establish a coordinate system. As the soft body inspection robot moves only in the XOY plane to cross the anti-vibration hammer, the torsion of the curve is zero. Additionally, due to the small bending angle of the robot's axis during the "Ω" movement, the bending shape can be approximated as a constant curvature arc shape. Thus, the motion of the coordinate system along the curve can be represented by Equation (10).

$$\begin{cases} \dfrac{d\boldsymbol{\alpha}(s)}{ds} = k\boldsymbol{\beta}(s) \\ \dfrac{d\boldsymbol{\beta}(s)}{ds} = -k\boldsymbol{\alpha}(s) \\ \dfrac{d\boldsymbol{\gamma}(s)}{ds} = 0 \end{cases} \tag{10}$$

5.2. Differential transformation of the position and posture of magnetically actuated soft inspection robot

Assuming that the curve is a constant curvature and the torsion is 0, deriving the first sub-equation in Eq. (10) and substituting the second sub-equation into the result of the derivative of the first sub-equation, the differential equation can be found as:

$$\boldsymbol{\alpha}'' + k\boldsymbol{\alpha} = 0 \tag{11}$$

The tangential vector equation is solved by bringing the initial conditions $\alpha_0 = \alpha(0)$ and $\beta_0 = \beta(0)$ into equation (10) as:

$$\boldsymbol{\alpha}(s) = \boldsymbol{\alpha}_0 \cos(ks) + \boldsymbol{\beta}_0 \sin(ks) \tag{12}$$

Integrating equation (12) over [0, s] yields:

$$\mathbf{x}(s) = \frac{\boldsymbol{\alpha}_0}{k}\sin(ks) + \frac{\boldsymbol{\beta}_0}{k}[1-\cos(ks)] \tag{13}$$

Assuming that $\boldsymbol{\alpha}_0 = \begin{pmatrix} \alpha_{0x} \\ \alpha_{0y} \\ 0 \end{pmatrix}$, it is observed from Fig. 17 that the unit tangent vector α, the principal normal vector β and the binormal vector γ follow the right-hand rule, the principal normal vector β can be obtained by rotating the unit tangent vector α clockwise around the binormal vector γ.

$$\boldsymbol{\beta}_0 = \begin{pmatrix} \cos(-\frac{\pi}{2}) & -\sin(-\frac{\pi}{2}) & 0 \\ \sin(-\frac{\pi}{2}) & \cos(-\frac{\pi}{2}) & 0 \\ 0 & 0 & 1 \end{pmatrix} \begin{pmatrix} \alpha_{0x} \\ \alpha_{0y} \\ 0 \end{pmatrix} = \begin{pmatrix} \alpha_{0y} \\ -\alpha_{0x} \\ 0 \end{pmatrix} \tag{14}$$

Taking α_0 and β_0 into equation (14) yields:

$$\|\mathbf{x}\| = \sqrt{\frac{1}{k^2}(\alpha_{0x}^2 + \alpha_{0y}^2)[\sin^2(ks) + 1 - 2\cos(ks) + \cos^2(ks)]} \tag{15}$$

Knowing $\|\boldsymbol{\alpha}\| = 1$, then $\alpha_{0x}^2 + \alpha_{0y}^2 = 1$, simplify formula (15) as:

$$\|\mathbf{x}\| = \frac{\sqrt{2}}{k}\sqrt{1-\cos(ks)} \tag{16}$$

Set the angle between α and **x** to be 30°,

$$\begin{cases} \sin\theta = \dfrac{\|\mathbf{x}\times\boldsymbol{\alpha}_0\|}{\|\mathbf{x}\|\|\boldsymbol{\alpha}_0\|} = \dfrac{\sqrt{2}}{2}\sqrt{1-\cos(ks)} \\ \cos\theta = \dfrac{\mathbf{x}\times\boldsymbol{\alpha}_0}{\|\mathbf{x}\|\|\boldsymbol{\alpha}_0\|} = \dfrac{\sqrt{2}}{2}\dfrac{\sin(ks)}{\sqrt{1-\cos(ks)}} \end{cases} \tag{17}$$

$$\theta = a\tan 2(\frac{\sqrt{2}}{2}\sqrt{1-\cos(ks)}, \frac{\sqrt{2}}{2}\frac{\sin(ks)}{\sqrt{1-\cos(ks)}}) = \frac{ks}{2} \tag{18}$$

Substituting formula (18) into (16) yields:

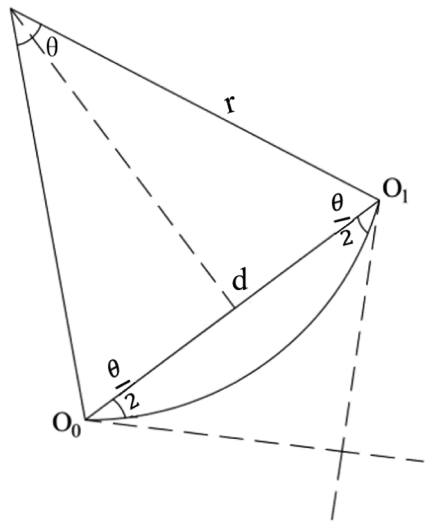

Fig. 18. Geometric relationship of single joint curve.

$$\|\mathbf{x}\| = \frac{s}{\theta}\sin\theta \tag{19}$$

From the above equations (19), the position vectors **x** of the base and tail nodes of the robot can be described.

5.3. Kinematic analysis of the "Ω" motion of the magnetically actuated soft inspection robot

Drawing the kinematics diagram of the single-section magnetically actuated soft inspection robot in Fig. 18, the "Ω" motion model of the robot can be simplified by connecting multiple sections in series [19]. A simplified model is shown in Fig. 19, where the translation in the z-axis direction is not considered (d = 0). By considering the rotational motion of the curve as a rotating joint, the magnetically actuated soft body inspection robot can be viewed as rotating at every point of the curve. To simplify the calculation of the "Ω" motion, the n "joints" are used to describe the "Ω" motion of the robot. For these "joints," forward kinematics can be calculated using the modified D-H method, as shown in Table 2.

The joint angle is known, so the robot end position and attitude can be obtained by calculation. ${}^{i-1}_{i}T$ is the transformation matrix of the coordinate system *i*-1 to the coordinate system *i*, coordinate system *i* can be obtained by performing four relative motions for coordinate system *i*-1:

$$\begin{aligned} {}^{i-1}_{i}T &= {}^{i-1}_{R}T\,{}^{R}_{Q}T\,{}^{Q}_{P}T\,{}^{P}_{i}T \\ &= T_{\hat{Z}_{i-1}}(\theta_i)T_{\hat{Z}_R}(d_i)T_{\hat{X}_Q}(a_i)T_{\hat{X}_P}(\alpha_i) \end{aligned} \tag{20}$$

The desired final position and posture is ${}^{0}_{n}T = {}^{0}_{1}T\,{}^{1}_{2}T\,{}^{2}_{3}T\,{}^{3}_{4}T\cdots{}^{n-1}_{n}T$. The matrix form of ${}^{n-1}_{n}T$ is:

$${}^{0}_{n}T = \begin{bmatrix} x_n & y_n & z_n & p_n \\ 0 & 0 & 0 & 1 \end{bmatrix} = \begin{bmatrix} n_x & o_x & a_x & p_x \\ n_y & o_y & a_y & p_y \\ n_z & o_z & a_z & p_z \\ 0 & 0 & 0 & 1 \end{bmatrix} \tag{21}$$

$$\begin{aligned} &n_x = c\theta_{12345678\cdots n} \quad o_x = -s\theta_{12345678\cdots n} \quad a_x = 0 \\ &p_x = a\left(c\theta_1 + c\theta_{12} + c\theta_{123} + c\theta_{1234} + \cdots + c\theta_{12345\cdots n}\right) \\ &n_y = s\theta_{12345678\cdots n} \quad o_y = c\theta_{12345678\cdots n} \quad a_y = 0 \\ &p_y = a\left(s\theta_1 + s\theta_{12} + s\theta_{123} + s\theta_{1234} + \cdots + s\theta_{12345\cdots n}\right) \\ &n_z = 0 \quad o_z = 0 \quad a_z = 1 \quad p_z = 0 \end{aligned}$$

5.4. Multi-segment magnetically actuated soft body inspection robot planar inverse kinematics

Multiplying both sides of Eq. (21) by ${}^{0}_{1}T^{-1}$, leads to the equation:

$${}^{0}_{1}T^{-1}\,{}^{0}_{n}T = {}^{0}_{1}T^{-1}\begin{bmatrix} n_x & o_x & a_x & p_x \\ n_y & o_y & a_y & p_y \\ n_z & o_z & a_z & p_z \\ 0 & 0 & 0 & 1 \end{bmatrix} \tag{22}$$

Substituting the formula ${}^{0}_{n}T = {}^{0}_{1}T\,{}^{1}_{2}T\,{}^{2}_{3}T\,{}^{3}_{4}T\cdots{}^{n-1}_{n}T$ into equation (22) yields:

$${}^{1}_{2}T\,{}^{2}_{3}T\,{}^{3}_{4}T\cdots{}^{n-1}_{n}T = \begin{bmatrix} n_x c\theta_1 + n_y s\theta_1 & o_x c\theta_1 + o_y s\theta_1 & a_x c\theta_1 + a_y s\theta_1 & p_x c\theta_1 - a + p_y s\theta_1 \\ n_y c\theta_1 - n_x s\theta_1 & o_y c\theta_1 - o_x s\theta_1 & a_y c\theta_1 - a_x s\theta_1 & p_y c\theta_1 - p_x s\theta_1 \\ n_z & o_z & a_z & p_z \\ 0 & 0 & 0 & 1 \end{bmatrix} \tag{23}$$

$$\begin{cases} a_x c\theta_1 + a_y s\theta_1 = 0 \\ a_y c\theta_1 - a_x s\theta_1 = 0 \end{cases} \tag{24}$$

$$(a_x + a_y)c\theta_1 + (a_y - a_x)s\theta_1 = 0 \tag{25}$$

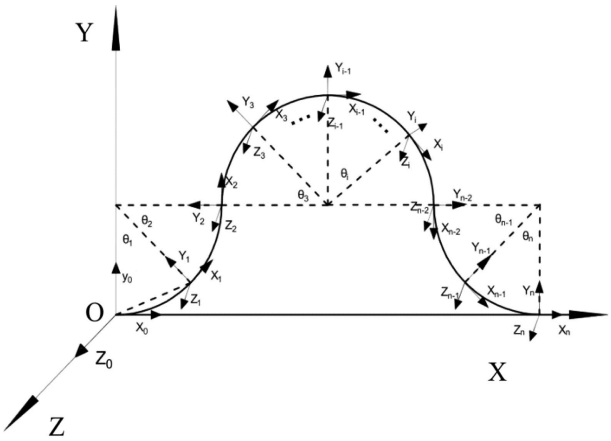

Fig. 19. "Ω" motion of n "joints".

Table 2. Multi-sectional curvilinear motion D-H table.

Link *i*	θ	d	a	α
1	θ_1	0	$2r_1\sin(\frac{\theta_1}{2})$	0
2	θ_2	0	$2r_2\sin(\frac{\theta_2}{2})$	0
3	θ_3	0	$2r_3\sin(\frac{\theta_3}{2})$	0
⋮	⋮	⋮	⋮	⋮
n	θ_n	0	$2r_n\sin(\frac{\theta_n}{2})$	0

Using the trigonometric identity transformation substitution formula, assume that

$$\begin{cases} \rho \sin\phi = a_y - a_x \\ \rho \cos\phi = a_y + a_x \end{cases} \tag{26}$$

$$\begin{aligned} &\rho\cos\phi s\theta_1 + \rho\sin\phi c\theta_1 = 0 \\ &\Rightarrow \sin(\phi+\theta_1) = 0 \\ &\Rightarrow \phi+\theta_1 = k\pi, \quad k \in Z \end{aligned} \tag{27}$$

$$\theta_1 = k\pi - \phi = k\pi - a\tan 2(a_y - a_x, a_y + a_x) \tag{28}$$

The remaining angles continue to be multiplied by ${}^1_2T^{-1}$, ${}^2_3T^{-1}$, ${}^3_4T^{-1}$, ${}^4_5T^{-1}$ $\cdots$ ${}^{n-2}_{n-1}T^{-1}$, to the left on the basis of the above method, and the angles θ_2, θ_3, θ_4, θ_n are obtained in turn.

5.5. Positive kinematics simulation of magnetically actuated soft inspection robot

Conventional rigid robots maintain a constant shape during motion, while soft robots have variable degrees of freedom that result in changes to their structure during motion [20]. To better visualize the overall curve structure during positive kinematic simulation, the size of the robot joints was reduced.

The number of "joints" to be taken as $n = 16$, and substituting the dimensional parameters of the soft robot into the calculation gives:

$$\begin{aligned} &l_{\text{arc}} = \frac{200}{16} = 12.5\text{mm} \\ &\text{r} = \frac{l_{\text{arc}}}{\alpha} = \frac{12.5\times 4}{\pi} \\ &l_{\text{chord}} = 2r\sin\left(\frac{\alpha}{2}\right) = 12.2mm \\ &\theta_1 = \theta_2 = \theta_3 = \theta_4 = \theta_{13} = \theta_{14} = \theta_{15} = \theta_{16} = \frac{\pi}{8} \\ &\theta_5 = \theta_6 = \theta_7 = \theta_8 = \theta_9 = \theta_{10} = \theta_{11} = \theta_{12} = -\frac{\pi}{8} \end{aligned} \tag{29}$$

The solution yields the final position and posture as:

$${}^0_{16}T = \begin{bmatrix} 1 & 0 & 0 & 122.67 \\ 0 & 1 & 0 & 0 \\ 0 & 0 & 1 & 0 \\ 0 & 0 & 0 & 1 \end{bmatrix} \tag{30}$$

The parameters mentioned above were input into Matlab, and the kinematic simulation was carried out using the robotics toolbox. By comparing the simulation results in Fig. 20 with the obstacle crossing action planning shown in Fig. 7(b), it was found that the two poses were identical and the transition of each joint is smooth, indicating that the results obtained from the kinematic equation were correct.

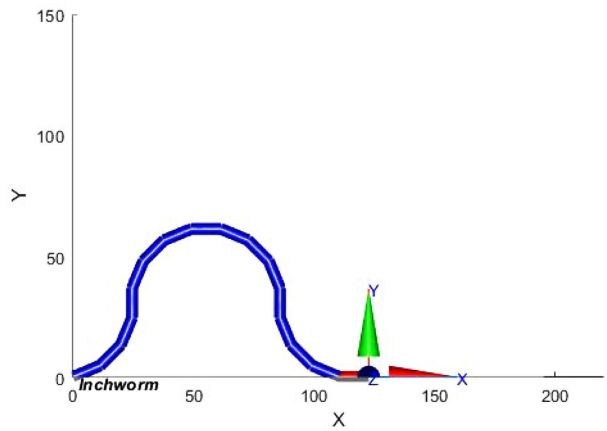

Fig. 20. (Color online) Simulation of "Ω" motion (Stage I).

To achieve the lifting motion when encountering an obstacle, the starting section's curvature needs to be increased, while the ending section's curvature needs to be decreased in stage I. Hence, the suggested angle is:

$$\begin{aligned} &\theta_{15} = \theta_{16} = \frac{\pi}{12} \\ &\theta_5 = \theta_6 = \theta_{11} = \theta_{12} = -\frac{\pi}{6} \\ &\theta_7 = \theta_8 = \theta_9 = \theta_{10} = -\frac{\pi}{8} \\ &\theta_1 = \theta_2 = \theta_3 = \theta_4 = \theta_{13} = \theta_{14} = \frac{\pi}{6} \end{aligned} \tag{31}$$

Other data do not need to be changed to solve for the final position and posture.

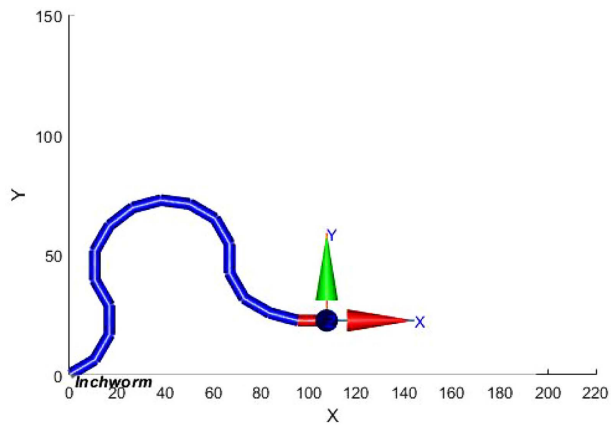

Fig. 21. (Color online) Simulation of "Ω" motion (Stage II).

$$ {}^{0}_{16}T = \begin{bmatrix} 1 & 0 & 0 & 107.54 \\ 0 & 1 & 0 & 22.50 \\ 0 & 0 & 1 & 0 \\ 0 & 0 & 0 & 1 \end{bmatrix} \tag{32} $$

After inputting the parameters into the robotics toolbox, a simulation diagram was obtained. The simulation results in Fig. 21 are in good agreement with the obstacle crossing action planning in Fig. 7(c), indicating the accuracy of the simulation.

The obstacle-crossing action finally presents a "Z" shape, the middle part of the peristaltic soft body is almost a straight line, at this point the arc length is equal to the chord length, i.e. the parameter a = 12.5 mm in the D-H table. The tilt angle is always constant during the rebound of the soft robot, and the parameters that change are as follows.

$$ \begin{aligned} &\theta_1 = \frac{\pi}{6} \\ &\theta_2 = \theta_3 = \cdots = \theta_{16} = 0 \\ &l_{\text{chord}} = l_{\text{arc}} = \frac{200}{16} = 12.5\text{mm} \end{aligned} \tag{33} $$

Final position and posture:

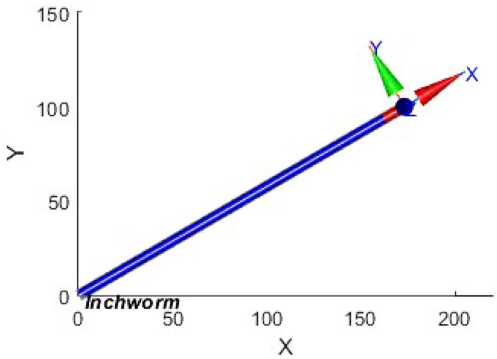

Fig. 22. (Color online) Simulation of "Ω" motion (Stage III).

$$ {}^{0}_{16}T = \begin{bmatrix} 0.87 & -0.5 & 0 & 173.21 \\ 0.5 & 0.87 & 0 & 100 \\ 0 & 0 & 1 & 0 \\ 0 & 0 & 0 & 1 \end{bmatrix} \tag{34} $$

The altered parameters were input into the initial Matlab program for simulation. The simulation results shown in Fig. 22 were compared with those in Fig. 7(d), and were found to be in excellent agreement, thereby validating the accuracy of the kinematic equation and the obstacle crossing action planning.

5.6. Inverse kinematics simulation of magnetically actuated soft body inspection robot

In order to achieve smoother motion and ensure continuity of velocity and acceleration, the joint space trajectory planning utilized the quintic polynomial interpolation method [21]. To obtain the robot motion trajectory, the initial angle θ_{initial} for each robot joint was set to 0 before the MATLAB simulation and then substituted into the termination angle θ_{target} for the three stages in Section 5.5. By applying these constraints, the simulation results were obtained.

With reference to the given joint rotation angle, the end trajectories of the three stages of the soft robot are planned. Fig. 23(a) shows the end trajectory of the contracted segment in stage I of the "Ω" motion, (b) is the end trajectory of the lifted section in stage II of the "Ω" motion, (c) shows the end trajectory of the straightened section in stage III of the "Ω" motion.

Fig. 24 is the joint position diagram, joint velocity diagram and joint acceleration diagram of the soft robot. From the following simulation diagram (40 steps per phase as a cycle), it can be seen that the soft robot movement is relatively smooth. Due to the particularity of the "Ω" shape, the joint motion curves may overlap.

Based on the kinematic parameter curve of the robot's obstacle-crossing joints presented above, all the robot's joints operate smoothly, which implies that there are no

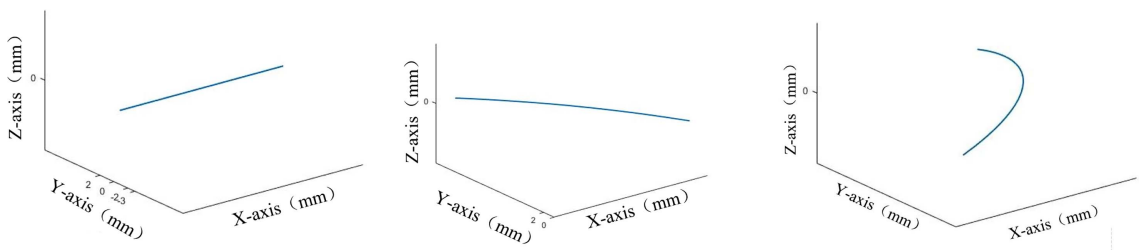

(a) Stage I (b) Stage II (c) Stage III

Fig. 23. (Color online) The end trajectory of the soft robot.

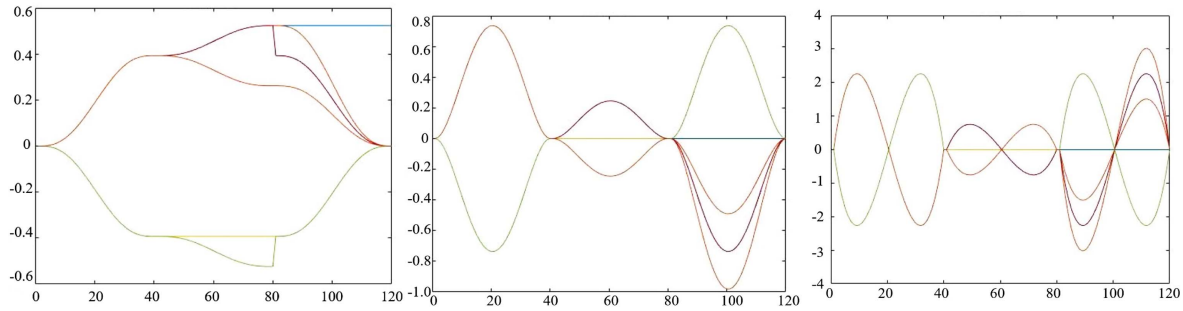

(a) Joint position in three stages (b) Joint velocity in three stages (c) Joint acceleration in three stages

Fig. 24. (Color online) Motion curve of each joint.

collisions or impacts, whether rigid or flexible, throughout the obstacle-crossing process of the line patrol robot. This finding validates that the structural parameters and design of the robot's obstacle-crossing gait are reasonable. Furthermore, the simulation analysis results confirm the accuracy of the kinematic model of the magnetically actuated HVDC transmission line's soft inspection robot.

6. Conclusion

This paper presents a novel magnetically actuated soft robot for high-voltage line inspection, which consists of three main components: a magnetic adsorber, a magnetic linear actuator, and a peristaltic soft body. The robot utilizes the ampere force generated by its own current-carrying coil in a toroidal reinforced magnetic field around a HVDC conductor to crawl over obstacles. Firstly, the magnetic field around the obstacles in the robot's working environment was simulated using COMSOL software, and it was found that the magnetic field had a circular shape around the obstacles. Based on this, models for the magnetic adsorber and magnetic linear actuator were developed, and the magnetic adsorption force and magnetic linear drive force were both theoretically calculated and simulated. The results showed a close agreement between the theoretical and simulated values, validating the correctness of the magnetic actuation principle. The paper concludes with the kinematic analysis and simulation of the "Ω"-shaped obstacle crossing action of the soft body robot, which imitates the inchworm. The results confirm the accuracy of the kinematic model for the magnetically actuated HVDC transmission line inspection robot. This research offers a crucial theoretical foundation for determining the optimal operating parameters and obstacle-crossing approach for the magnetically actuated soft robot utilized in high-voltage line inspection tasks.

References

[1] P. Debenest, M. Guarnieri, K. Takita, E. F. Fukushima, S. Hirose, K. Tamura, A. Kimura, H. Kubokawa, N. Iwama, and F. Shiga, Proc. IEEE Intl.Conf. Rbt. Auto. 3978 (2008).

[2] N. Pouliot and S. Montambault, Proc. ICRA. 3970 (2008).

[3] N. Pouliot, P. L. Richard, and S. Montambault, IEEE Pwr. Nrg. Tech. Sys. J. **2**, 1 (2015).

[4] K. Toussaint, N. Pouliot, and S. Montambault, J. Field Rob. **26**, 411 (2009).

[5] G. P. Wu, X. Xiao, Y. L. Guo, and J. C. Hu, China. Mech. Eng. **17**, 237 (2006).

[6] C. L. Sun, H. G. Wang, and M. Y. Zhao, China. Mech. Eng. **18**, 4 (2007).

[7] Y. Chen, L. Wang, K. Galloway, I. Godage, N. Simaan, and E. Barth, Soft Rob. **8**, 298 (2021).

[8] J. D. Hubbard, R. Acevedo, K. M. Edwards, A. T. Alsharhan, Z. Wen, J. Landry, K. Wang, S. Schaffer, and R. D. Sochol, Sci. Adv. **7**, 5257 (2021).

[9] B. McInroe, H. C. Astley, C. Gong, S. M. Kawano, P. E. Schiebel, J. M. Rieser, H. Choset, R. W. Blob, and D. I. Goldman, Sci. Adv. **353**, 154 (2016).

[10] D. Rus and M. T. Tolley, Nature **521**, 467 (2015).

[11] T. George, Y. Ansari, and E. Falotico, Soft. Rob. **5**, 149 (2018).

[12] J. Yang, H. Peng, W. Zhou, J. Zhang, and Z. Wu, Mech. Mach. Theory. **165**, 104429 (2021).

[13] X. J. Xu, L. L.Wu and X. J. Yang, and J. Zhejiang, Univ. (Eng. Sci.). **50**, 1938 (2016).

[14] X. J. Xu, Y. L. Feng, L. Fang and X. L. Yang, Mach. Desg. Manuf. **5**, 61 (2016).

[15] X. J. Xu, C. H. Liu, Y. Yan, L. Fang, Y. L. Wang, and L. H. Wu, J. Magn. **23**, 423 (2018).

[16] W. Wang, G. P. Wu, Y. C. Bai, H. Xiao, Z. Y. Yang, Y. Yan, Y. He, X. J. Xu, and F. Su, J. Cent. South. Univ. **21**, 2216 (2014).

[17] X. J. Xu, Y. H. Yang, H. Chen, L. Liu, and Y. Yan, J. Magn. **26**, 87 (2021).

[18] E. B. Joyee and Y. Pan, Soft. Rob. **6**, 333 (2019).
[19] R. K. Katzschmann, C. D. Santina, Y. Toshimitsu, A. Bicchi, and D. Rus, IEEE Intl. Conf. Soft Rob, 454 (2019).
[20] K. Zimmermann, V. Naletova, I. Zeidis, V. Turkov, E. Kolev, M. Lukashevich, and G. Stepanov, J. Magn. Magn. Mater. **311**, 450 (2007).
[21] X. C. Li, Master. Thesis, Hunan University of Technology, China (2022).